
THE CHANGING RULE OF HUMAN BONE DENSITY WITH AGING BASED ON A NOVEL DEFINITION AND MENSURATION OF BONE DENSITY WITH COMPUTED TOMOGRAPHY

Linmi Tao*[✉], **Ruiyang Liu***, **Yuanbiao Wang**, **Yuezhi Zhou**
Department of Computer Science and Technology
Tsinghua University
linmi@tsinghua.edu.cn

Li Huo[✉], **Guilan Hu**
Nuclear Medicine Department
Peking Union Medical College Hospital
huoli@pumch.cn

Xiangsong Zhang
Department of Nuclear Medicine
First Affiliated Hospital of Sun Yat-sen University

Zuo-Xiang He[✉]
School of Clinical Medicine
Beijing Tsinghua Changgung Hospital
zuoxianghe@tsinghua.edu.cn

*Co-first author.

✉Corresponding author.

ABSTRACT

Osteoporosis and fragility fractures have emerged as major public health concerns in an aging population. However, measuring age-related changes in bone density using dual-energy X-ray absorptiometry has limited personalized risk assessment due to susceptibility to interference from various factors. In this study, we propose an innovative statistical model of bone pixel distribution in fine-segmented computed tomography (CT) images, along with a novel approach to measuring bone density based on CT values of bone pixels. Our findings indicate that bone density exhibits a linear decline with age during adulthood between the ages of 39 and 80, with the rate of decline being approximately 1.6 times faster in women than in men. This contradicts the widely accepted notion that bone density starts declining in women at menopause and in men at around 50 years of age. The linearity of age-related changes provides further insights into the dynamics of the aging human body. Consequently, our findings suggest that the definition of osteoporosis by the World Health Organization should be revised to the standard deviation of age-based bone density. Furthermore, these results open up new avenues for research in bone health care and clinical investigation of osteoporosis.

Keywords Bone density · Osteoporosis · Computerized tomography

1 Introduction

Fragility fractures are associated with high levels of disability and mortality in the elderly. The early identification of fracture risk by non-invasive quantitative analysis followed by effective intervention can significantly reduce the burden and costs of osteoporosis. The World Health Organization (WHO) defines osteoporosis in postmenopausal women and men over the age of 50 based on dual-energy X-ray absorption. According to their definition, osteoporosis is characterized by a reduction in bone density exceeding 2.5 standard deviations (-2.5 SD) from the peak bone mass of healthy young individuals of the same gender, or the occurrence of fragility fractures [1]. However, age-related changes in bone density, as determined by dual-energy X-ray absorptiometry, may not completely indicate personalized risk due to susceptibility to interference from various other factors [2, 3]. As described in the existing literature, the concept that bone mineral density shows a significantly high rate of decline with age [4], or over a few years [5], may not be a

The changing rule of human bone density with aging based on a novel definition and mensuration of bone density with computed tomography

universal rule for the changes in human bone density, but may actually represent errors caused by various factors such as measurement methodology and disease in the observed population. Thus, the scientific foundation and accuracy of the WHO's definition of osteoporosis are subject to question.

In clinical practice, bone density can be assessed using low-energy computed tomography on Positron Emission Tomography/Computed Tomography (PET/CT) [6, 7], which measures the volumetric bone density with an accuracy in the range of cubic millimeters (mm^3). CT-based measurements can eliminate the influence of surrounding soft tissues, calcification, and bone degeneration on bone density, while also aiding in the detection of other diseases [8]. In addition, CT values are consistent between different devices, thus increasing the reliability and feasibility of this technique. The primary challenge in expanding the use of PET/CT for quantifying bone density is the accurate selection of bone segment images and obtaining a representative bone density measurement through modeling the distribution of the acquired segment CT pixels.

2 Materials and Results

In order to maintain independent sampling and minimize the impact of different imaging equipment on the experimental results, we gathered CT images from 1,641 patients who underwent whole-body PET/CT examinations at Peking Union Medical College Hospital (referred to as N Hospital) in Beijing, as well as the First Affiliated Hospital of Sun Yat-sen University (referred to as S Hospital) in Guangzhou, which are situated in northern and southern China, respectively. From the collected CT images, we created two distinct datasets: (1) the CT images of 750 patients at N Hospital had a resolution of 512×512 pixels and a slice thickness of 3 millimeters, and (2) the CT images of 891 patients at S Hospital had a resolution of 512×512 pixels and a slice thickness of 5 millimeters.

We developed a deep neural network using the created datasets (see Supplementary Section B) to accurately classify bone segments in CT images as either cortical or cancellous. The Johnson-Su function* was used to statistically fit the pixels in the segmented area. The CT pixel value at the maximum point of the function represented the bone density measurement for that segmented area. The cancellous bone of the L1 and L2 vertebral bodies was chosen as the representative bone to calculate the overall bone density of the human body, based on previous research [5, 9], existing guidelines [7], and our clinical experience with numerical analysis.

Due to the limited number of cases below the age of 39 and above the age of 80, our study focused on analyzing 1,018 cases between the ages of 39 and 80. The dataset included 434 cases from N Hospital and 584 cases from S Hospital (Supplementary Figure 5). Subsequently, we developed an equation (Equation (1) – (3)) to characterize the change in bone density with age. Our analysis revealed a consistent linear decline in bone density among adults between the ages of 39 and 80 as age increased (Figure 1). Overall, women experienced a more rapid decline in bone density compared to men. Our calculations indicated that the average rate of bone mineral density decline was approximately 1.6 times faster in women than in men. Additionally, our findings revealed geographical variations in the decline rates among men. Specifically, the decline rate at N Hospital was 1.35 times faster than that at S Hospital. However, the rate of decline in women was consistent across both hospitals. This geographical variation is comparable to that of obesity in China [10].

3 Mensuration of bone density

We compiled a collection of over 20 segmentation networks and created a segmentation model library called JMedSeg (Jittor Medical Segmentation [11]). This library enabled the precise selection of cancellous bone segments at a sub-pixel level [12] (Supplementary Section B). Using the acquired pixels, we applied the Johnson-Su function to model their distribution within a segment. By examining the resulting model function, we defined the CT value at the maximum point of the function as an indicator of the bone mineral density for the specific segment of cortical or cancellous bone (Figure 2, Supplementary Figure 6). This definition of the measurement approach provides an estimation of bone mineral density by approximating CT pixel data values. As a result, it showcases the significance of utilizing CT for bone density assessment.

We conducted a comprehensive analysis of various bones, ranging from the skull to the femur, to assess their density using this innovative measurement technique. Additionally, we examined how bone density changes with age. Through statistical analysis of the datasets, we determined that the cortical bone density in adults averaged approximately 2,500 CT Units (Hu), while the bone marrow density averaged around 1,000 Hu. It is important to note that both parameters remained consistent and were not influenced by gender or age. Furthermore, we discovered that the density of cancellous bone in the lumbar vertebrae showed variation within a specific range (Supplementary Figure 7).

*<https://docs.scipy.org/doc/scipy/reference/generated/scipy.stats.johnsonsu.html>

Previous clinical studies have demonstrated that cancellous bone has a rich blood supply and a large surface area, resulting in a higher rate of bone turnover compared to cortical bone [13]. During the initial phases of osteoporosis, bone loss predominantly takes place in cancellous bone. Consequently, the vertebral bodies, which contain a significant amount of cancellous bone, are frequently impacted by osteoporosis. Furthermore, given its role as a weight-bearing structure, fractures caused by osteoporosis are frequently observed in the thoracolumbar spine [14]. Notably, both the 2018 China Guidelines [7] and previous studies [5, 9, 15] have highlighted the lumbar spine as a crucial area for osteoporosis evaluation.

Through a deeper examination of the vertebral CT images, we observed that the L1 and L2 vertebral bodies exhibited a higher amount of cancellous bone and less deformation in comparison to the L3-L5 bodies and other bones. Therefore, we recommend measuring bone density specifically in the cancellous bone of the L1 and L2 vertebral bodies.

4 The changing rule of bone density with aging

To ensure a sufficient number of pixels for robust statistical analysis, we aggregated data from all individuals within a 3-year range and formed a single group. For example, individuals aged 39, 40, and 41 were classified into the 40-year group. Using our proposed definition and measurement of bone density, there are two analytical methods to estimate the mean bone density for a specific age: (1) Group statistics, which employs all data within an age group to estimate the bone density for that age; (2) Personal statistics, which utilizes data from each individual to estimate their personal bone density, and then aggregates all personal bone density values into a 3-year age group. Subsequently, we calculated bone mineral density values and modeled their changes with age (see Figure 3). The analysis revealed a gradual linear decline in bone density among adults as they age, with women generally experiencing a faster decline compared to men. This linear change in bone density is described by Equation (1).

$$\begin{cases} D_{MN} = -k_{MN}A + Z_{MN} \\ D_{MS} = -k_{MS}A + Z_{MS} \\ D_{FN} = -k_{FN}A + Z_{FN} \\ D_{FS} = -k_{FS}A + Z_{FS} \end{cases} \quad (1)$$

Equation (1) describes the relationship between bone density D , age A , the rate of decline in bone density k , and the baseline offset for bone density Z , which are differentiated by subscripts M (Male), F (Female), N (N-hospital), and S (S-hospital). By fitting a line to the data on mineral density (Figure 3), we were able to determine the variations in bone density with increasing age, as depicted by Equation (2) and Table 1.

$$\begin{cases} D_{MN} = -2.62A + 1314.88 \\ D_{MS} = -1.94A + 1277.66 \\ D_{FN} = -3.66A + 1361.28 \\ D_{FS} = -3.69A + 1367.20 \end{cases} \quad (2)$$

Table 1: The coefficient of determination (R^2) and standard variance between the fitted Equation (2) and the data points.

	MN*	MS*	FN*	FS*
Coefficient of determination (R^2)	0.9	0.88	0.97	0.92
Standard variance (Hu)	3.79	3.36	3.32	4.41

* M: Male, F: Female, N: N-hospital, S: S-hospital

To examine the impact of the dataset on the equation for bone mineral density, we computed the bone density for each individual based on the collected dataset. We derived Equation (3) and Table 2, which illustrate the variations in bone density with age (Figure 4(a) and 4(b)), respectively.

$$\begin{cases} D_{MN} = -2.34A + 1296.30 \\ D_{MS} = -1.86A + 1271.49 \\ D_{FN} = -3.54A + 1354.93 \\ D_{FS} = -3.59A + 1358.96 \end{cases} \quad (3)$$

Equations (2) and (3) highlight the essential parameters (k_{FN} , k_{FS} , k_{MN} , k_{MS}) that clearly demonstrate a reduction in bone mineral density of approximately 3.6 CT Units per year (Hu/yr) among women in both hospitals. For men,

Table 2: The standard variance between the fitted Equation (3) and the data points.

	MN*	MS*	FN*	FS*
Standard variance (Hu)	5.84	5.81	5.74	6.24

* M: Male, F: Female, N: N-hospital, S: S-hospital

the rates of decline in N hospital and S hospital were 2.5 Hu/yr and 1.9 Hu/yr, respectively. Alternatively, these declining rates can be expressed as a more conventional percentage per year, namely 0.3% for women and 0.2% for men (see Figure 4(c)). The coefficient of determination for the fitting (refer to Table 1) and its standard variance (Table 1 and 2) indicate a good fit of the linear model to the data. These findings are further supported by resampling (refer to Supplementary Figure 8).

Utilizing these equations, we determined the average ratio for the rate of decline between men and women ($(k_{MN} + k_{MS}) / (k_{FN} + k_{FS})$), revealing that women experience a 1.6-fold faster decline in bone density compared to men. Figures 1 and 4 visually depict the observation that women generally experience less decline in bone density than men, particularly around the age of 50, as clearly demonstrated in Figures 4(c) and 4(d). This finding aligns with the clinical observation that osteoporosis is more prevalent among older women.

Furthermore, our analysis revealed a notable disparity in the rate of decline in bone density between men from northern and southern hospitals, with a ratio of 1.3. This suggests that men residing in northern China may experience a faster decline in bone density compared to their counterparts in the south. Remarkably, this study is the first to identify regional distinctions in the rate of bone density decline.

5 Conclusion

The definition of bone density and the estimations derived from our analytical approach reveal that bone mineral density exhibits a linear pattern with age during adulthood between the ages of 39 and 80, without displaying an accelerated decline associated with menopause in women or within a specific age range in men. Based on the framework we developed to assess bone density decline, the cumulative decline over a span of 40 years (from 40 to 79 years of age) was observed to be 11.4% in women and 6.8% in men. These findings suggest the need for revising the current World Health Organization (WHO) definition of osteoporosis, which currently relies on peak bone density.

The AI-based methodology presented in this study represents a significant advancement and modernization in the field of bone density measurement, departing from the conventional dual-energy X-ray absorptiometry approach. Instead of relying on rough estimations based on whole-body absorption, our method enables precise and separate measurements of cortical, cancellous, and marrow bone. Notably, the measurement of the human body at L1 and L2 yields a new physiological index that can serve as an indicator of overall health. Additionally, the observed linear decline in bone density serves as a valuable tool for understanding the dynamics of aging within the body. These groundbreaking findings have opened up new avenues for researchers in the realm of clinical osteoporosis diagnosis through the utilization of CT scanning.

Data and code availability

No human or animal subject was used in this study. All the data used in this study are available publicly in outpatient departments of both N hospital and S hospital.

We reproduce most variants of segmentation models in Jittor. Code is available at <https://github.com/THU-CV1ab/JMedSegV2>.

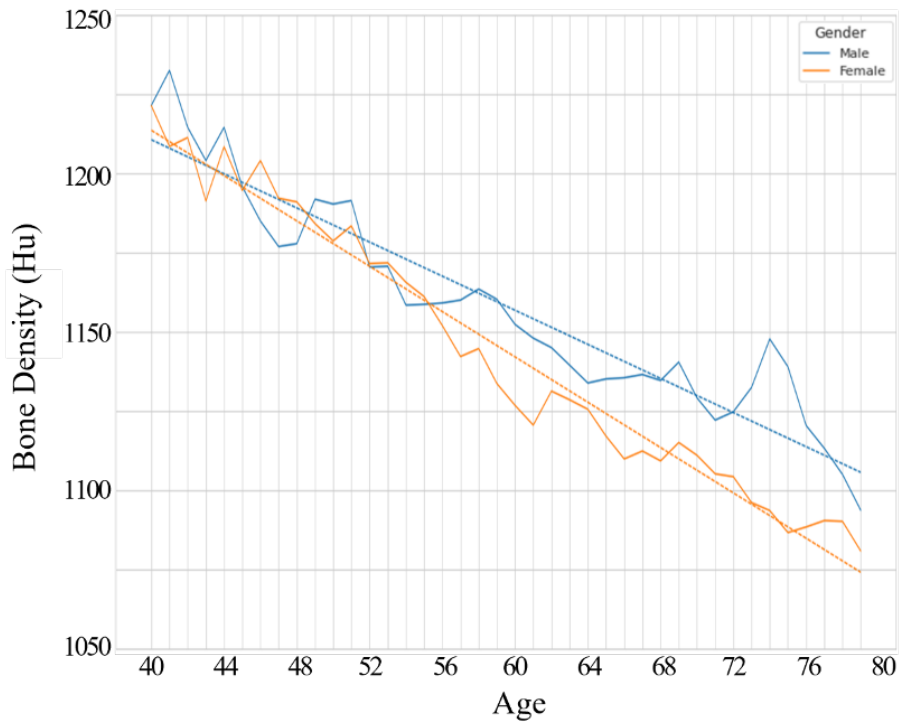
Acknowledgment

We deeply thank all the students of the courses ‘‘Pattern Recognition’’ 2021 and 2022, Department of Computer Science and Technology, Tsinghua University, for their contribution to the development of the segmentation models.

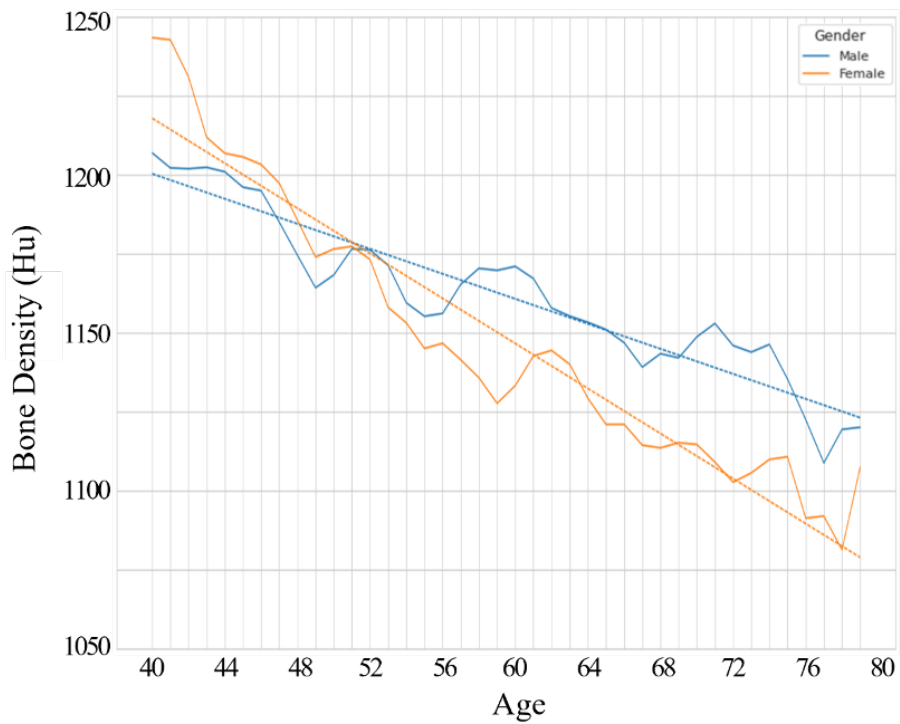
We thank Mr. Zhoujie Fu, the student of Department of Computer Science and Technology, Tsinghua University, for his contribution to the development of the interface of deep learning based segmentation, and part of the models as well.

We thank to the National Natural Science Foundation (Details will be added) and Tsinghua University for their funds to this research.

The changing rule of human bone density with aging based on a novel definition and mensuration of bone density with computed tomography



(a) N Hospital



(b) S Hospital

Figure 1: The bone density-age curves demonstrate a consistent decline in bone density with age. The bone density is measured using precise segmentation of the cancellous bone of L1 and L2 vertebral bodies, obtained from CT data collected from N and S hospitals.

The changing rule of human bone density with aging based on a novel definition and mensuration of bone density with computed tomography

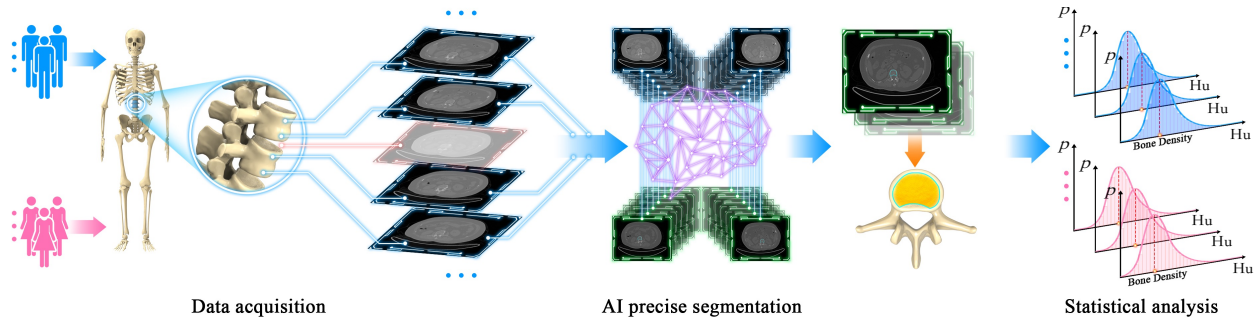


Figure 2: The process of novel mensuration of bone density. CT images were obtained by scanning lumbar vertebrae L1 and L2 during the data acquisition stage. The cancellous bone was precisely segmented using a neural network during the AI-based segmentation stage. The Johnson-Su statistical model is fitted to the distribution of segmented bone pixels during the statistical analysis stage. The CT value corresponding to the peak of the model is defined as the measure of bone density.

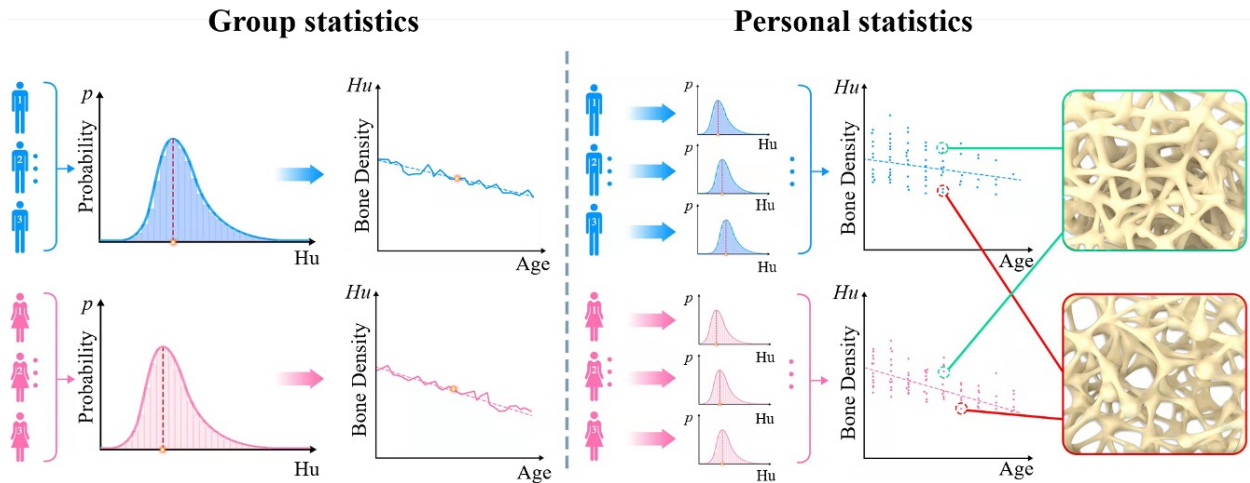
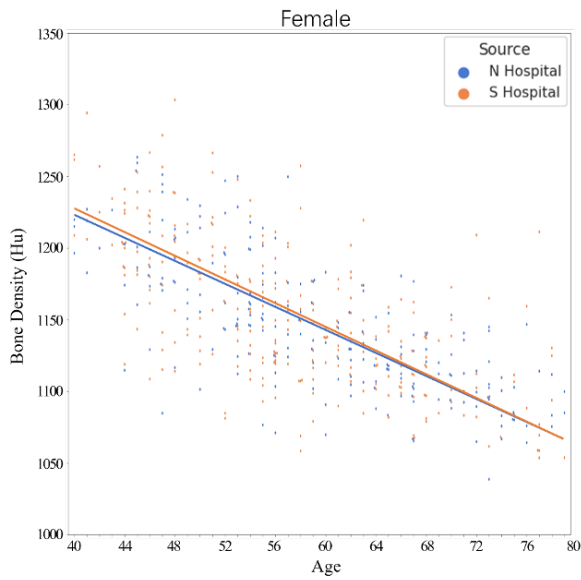
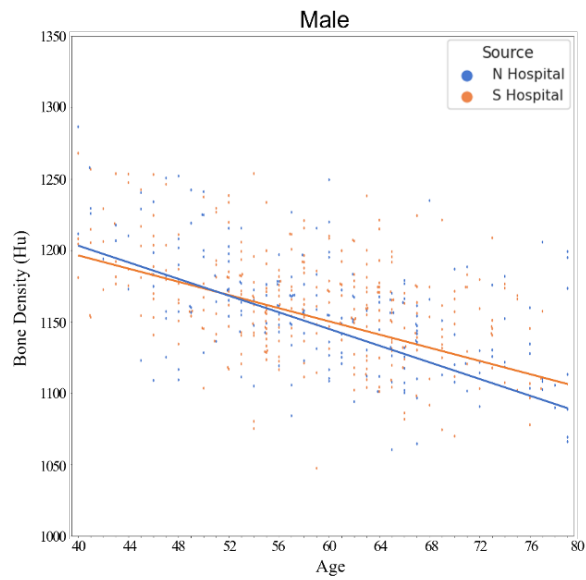


Figure 3: The process of identifying patterns in bone density changes with age. Bone density at a specific age was determined using both group statistics (average values within a 3-year age range) and personal statistics (individual measurements within a 3-year age group). Statistical models were fitted to the estimated bone density, providing evidence of a linear decline in bone density with increasing age.

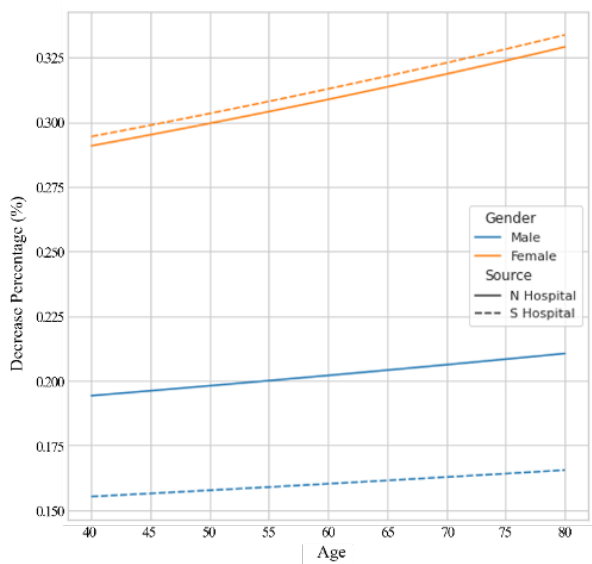
The changing rule of human bone density with aging based on a novel definition and mensuration of bone density with computed tomography



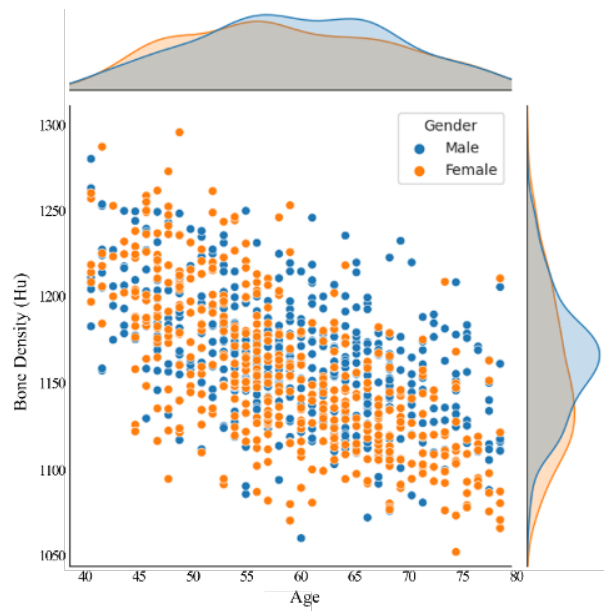
(a) Female bone mineral density distribution



(b) Male bone mineral density distribution



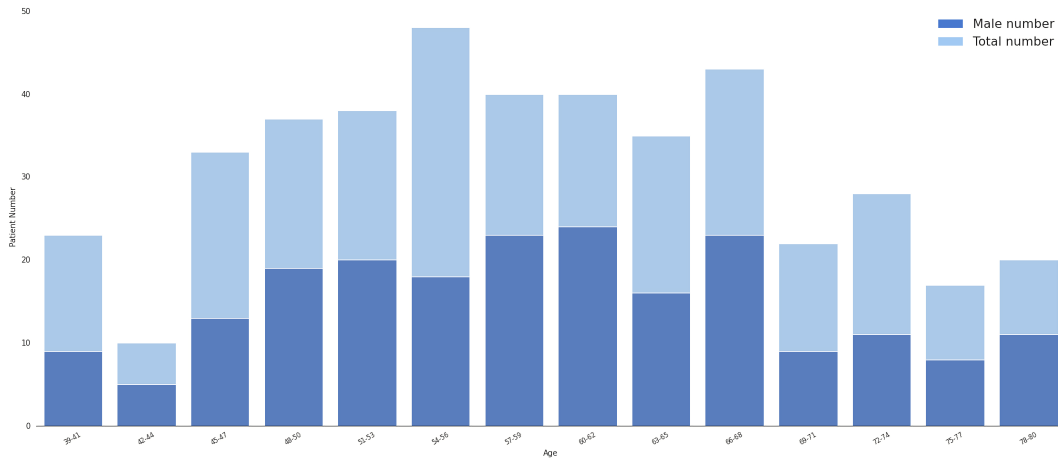
(c) The rule of bone density changes with age in percentage



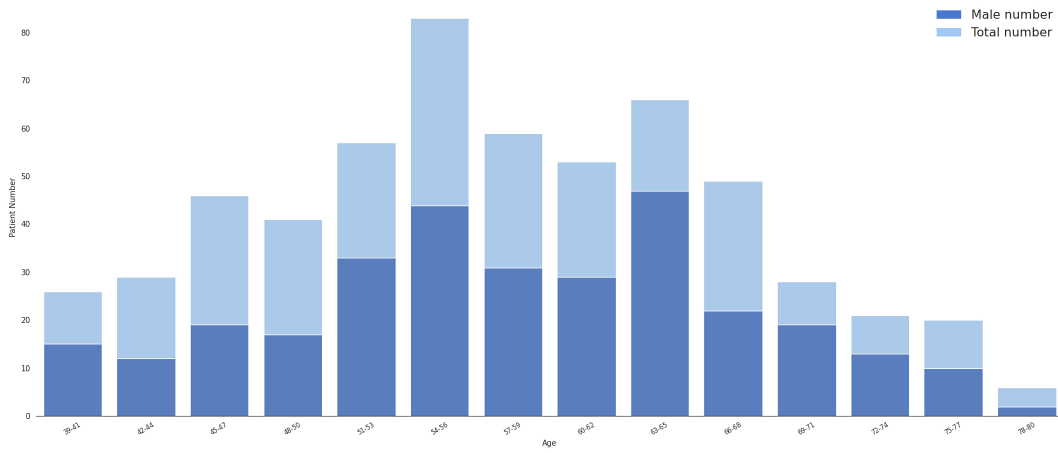
(d) Overall bone mineral density distribution

Figure 4: The distribution of bone mineral density per person as a function of age was analyzed. Blue dots indicate patients from S hospital, while orange dots indicate patients from N hospital.

A Supplementary Figures



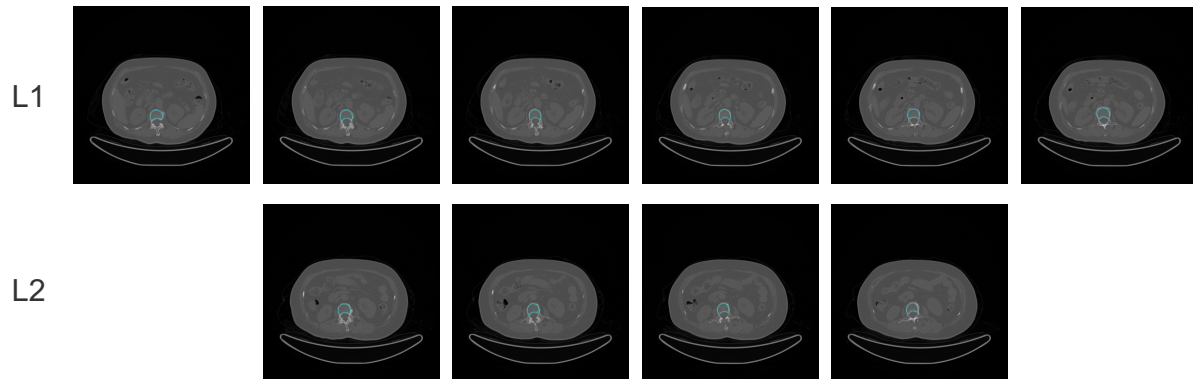
(a) N Hospital



(b) S Hospital

Figure 5: The number and age distribution of men and women in the two independent datasets collected in the N and S hospitals. The dark blue part indicates men, and the non-overlapping light blue part refers to women. The men-to-women ratio in our dataset is approximately 1 : 1.

The changing rule of human bone density with aging based on a novel definition and mensuration of bone density with computed tomography



(a) Cancellous bone segmented in CT images

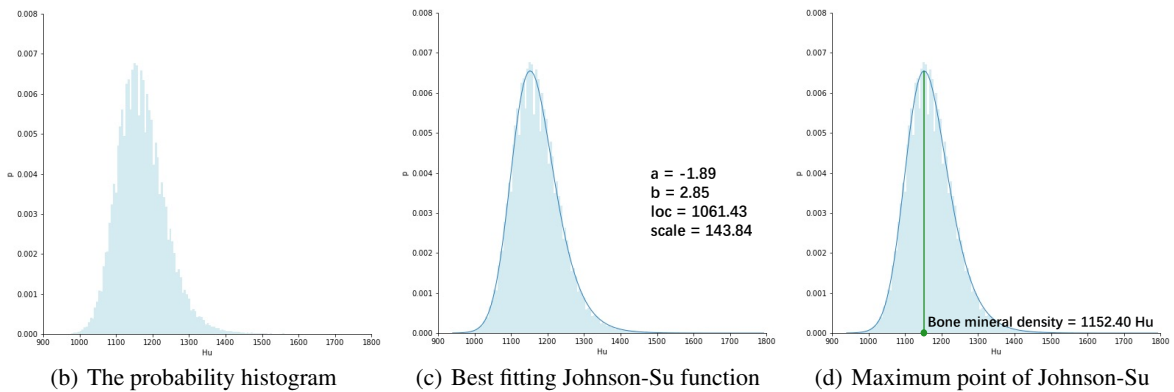


Figure 6: The process of calculating the bone density value. (a) The cancellous bone zones are separated from L1 and L2 vertebral bodies on CT images. The sub-figures show all the CT images of L1 and L2 of a case at N hospital. (b) The probability histogram of the values of CT pixels in the cancellous bone zones, in which the horizontal coordinate is the CT value (Hu) and the vertical coordinate is the probability density (p). (c) The best fitting of a Johnson-Su function to the probability histogram is calculated with parameters a , b , loc , and $scale$. (d) The point at the horizontal coordinate related to the maximum value of the Johnson-Su function is calculated and its value is defined as the bone density.

The changing rule of human bone density with aging based on a novel definition and mensuration of bone density with computed tomography

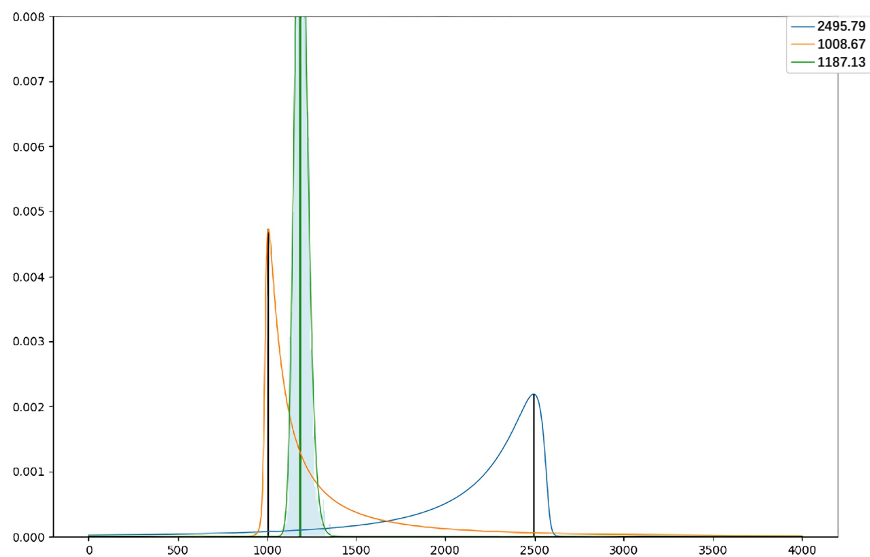
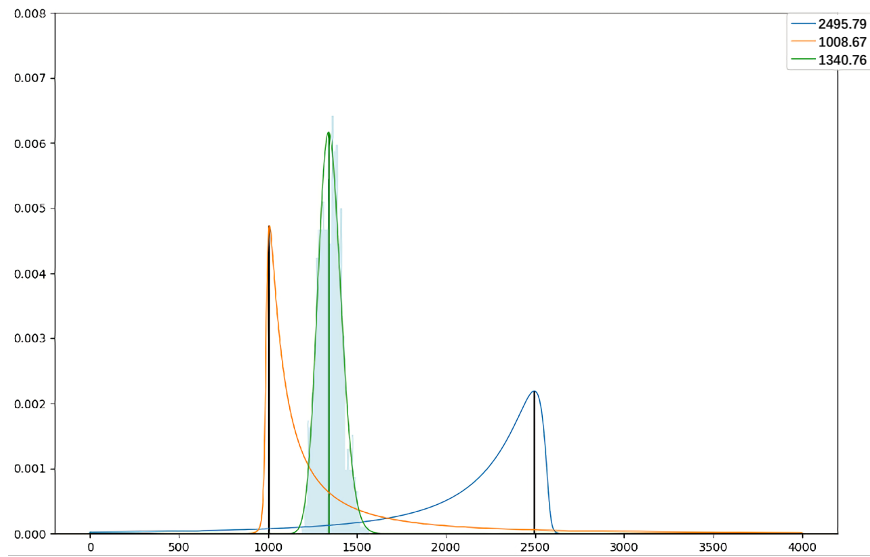


Figure 7: Histogram of the lumbar spine (green) and the function fitted by Johnson-Su (green curve). Bone density is defined as the CT value (indicated by the vertical line) at the maximum value of the fitted curve. In the figure, the orange curve is the fitting function of the femoral marrow, and the vertical line indicates the bone marrow density. The blue curve is the fitting function of the femoral cortex, and the vertical line indicates the bone cortex density. These two bone density values are used to calibrate the maximum value (bone cortex) and the minimum value (bone marrow) of bone density. The green curve in the middle is the bone density of the lumbar spine. The bone density values are written in the upper right corner. It can be seen from the figure that the bone density of the lumbar spine changes with the individual.

The changing rule of human bone density with aging based on a novel definition and mensuration of bone density with computed tomography

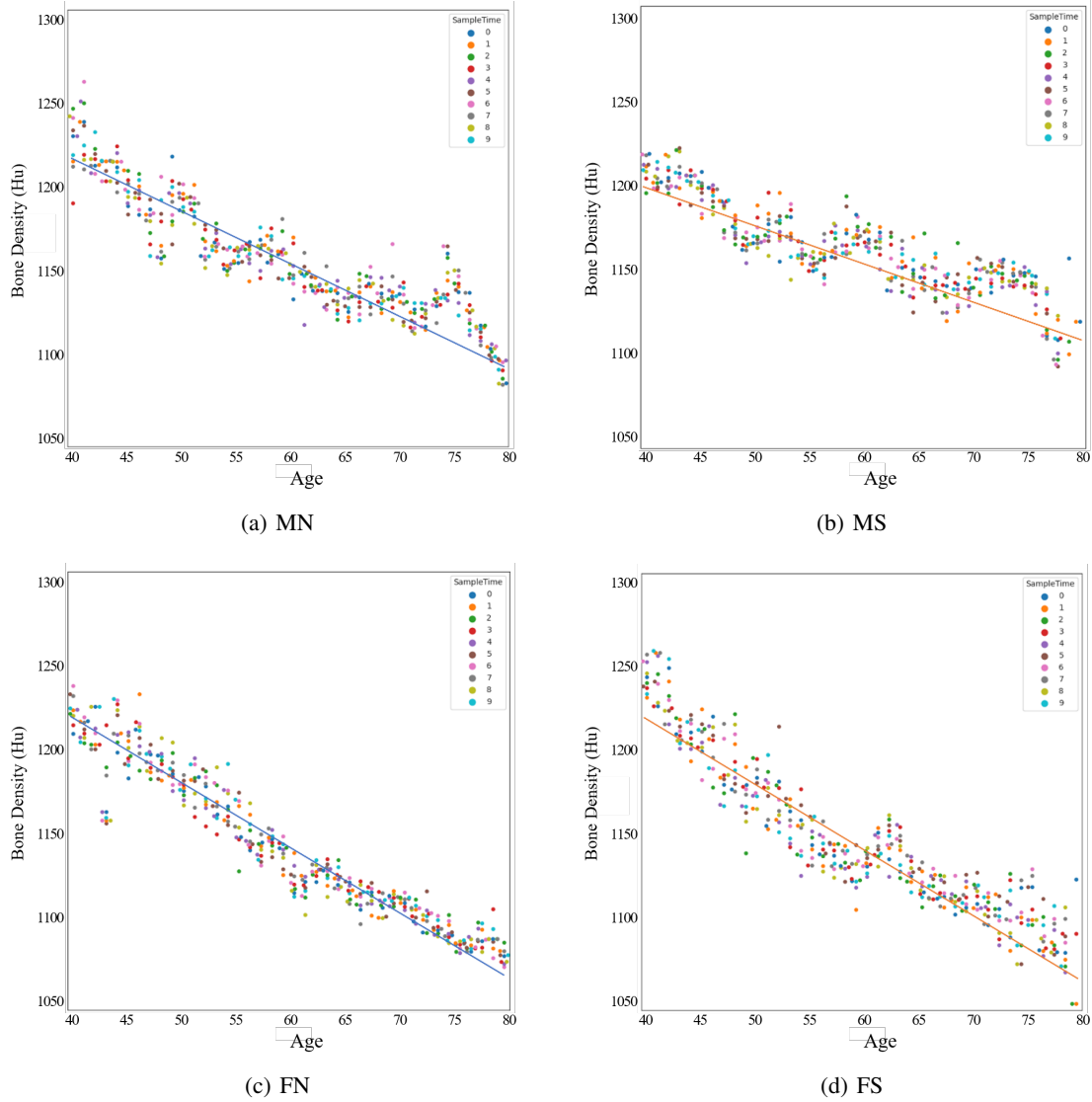


Figure 8: Bone density distribution with age based on random sampling, where M: Male, F: Female, N: N Hospital, S: S Hospital. The straight lines in different colors represent the bone density equations fitted for each sample. We used resampled data from N and S hospitals to investigate changes in the bone mineral density of men and women under identical sampling conditions. We carried out 10 repeated samplings of 10 people on each occasion, and obtained equation for changes in bone density with age, where D is bone density and A is age:

$$\begin{cases} D_{MN} = -2.66A + 1316.43 \\ D_{MS} = -1.97A + 1278.55 \\ D_{FN} = -3.51A + 1352.47 \\ D_{FS} = -3.59A + 1360.74 \end{cases}$$

B Supplementary Method

B.1 Deep Learning Model Backbone Selection

In recent years, end-to-end deep learning has emerged as the dominant approach for image semantic segmentation. Treating the segmentation problem as a pixel-wise classification task enables researchers to achieve favorable results using well-established deep neural networks [16, 17, 18, 19]. Among various segmentation tasks, medical image segmentation stands as a vital application.

The UNet [20] architecture, which gained significant recognition, was proposed in 2015. It utilizes symmetrical downsampling and upsampling modules to achieve end-to-end medical image segmentation. Multiple convolutions, pooling, and activations are applied by UNet to obtain multi-channel feature maps at reduced scales. Subsequent upsampling operations are then conducted to produce a binary map of the input image size for pixel-wise segmentation. Moreover, UNet incorporates skip-connections that leverage high-level semantic information from multiple stages, thereby alleviating the training process’s complexity. The architecture of UNet is visually depicted in Figure 9.

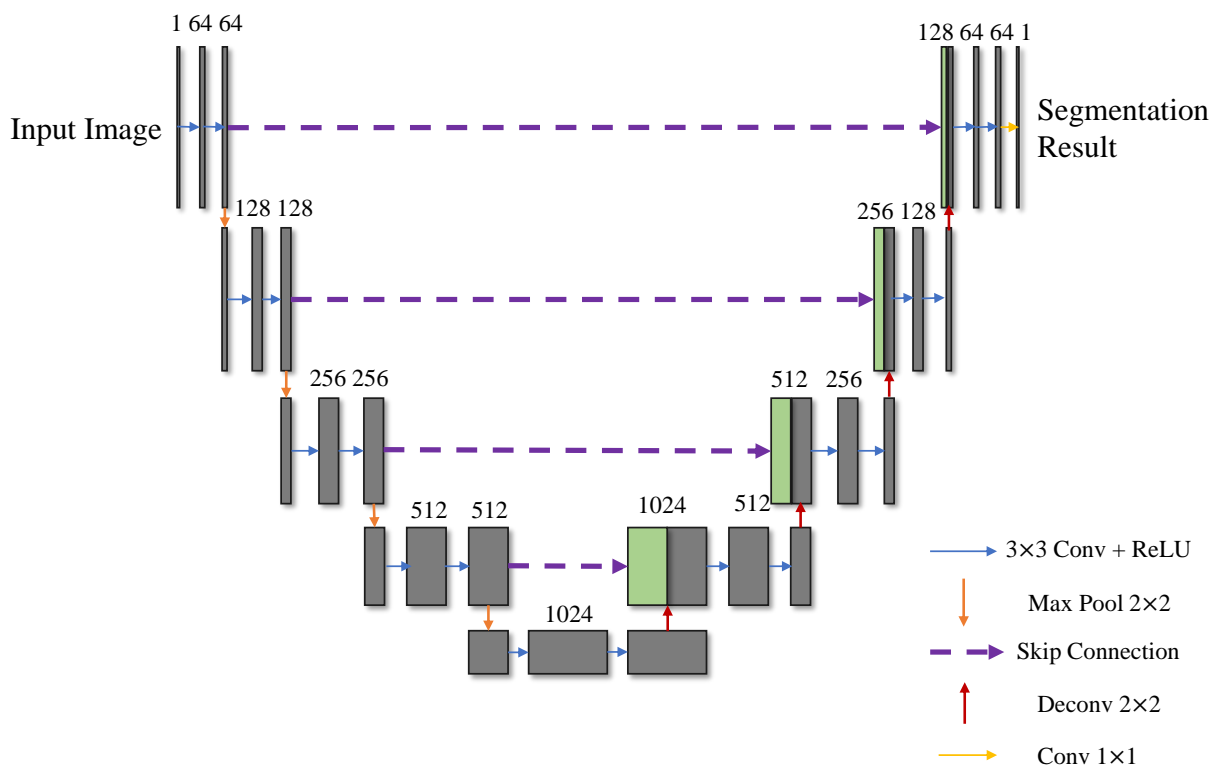


Figure 9: UNet structure.

UNet has been a fundamental deep learning structure in medical segmentation since its first launch. Many experiments [21, 22, 23, 24] have verified its validity, spurring several CNN models with similar downsample-upsample infrastructure to be applied to semantic segmentation. For instance, UNet++ [25] and UNet3+ [26] explored more intricate structural designs to substitute the skip-connection. U²Net [27] proposed the adoption of a nested UNet-like structure for the downsampling and upsampling modules, whereas the DeepLab [28] series substituted the conventional convolution with dilated convolution. ResUNet [29] and DenseUNet [30] employed large pre-trained networks as the downsampling backbone, while DANet [31] incorporated an attention mechanism to enhance its performance, and SETR [32] utilized the transformer encoder-decoder blocks. We perform comprehensive benchmarking experiments utilizing Jittor [11], a high-performance deep learning framework, to identify the optimal deep learning network for

The changing rule of human bone density with aging based on a novel definition and mensuration of bone density with computed tomography

our task. Furthermore, we have compiled over 20 segmentation networks and developed a segmentation model library named **JMedSeg** (**J**ittor **M**edical **S**egmentation)[†].

Based on the preliminary experimental results, we conclude that despite variations in performance on public datasets, UNet achieves comparable results with significantly fewer parameters. Additionally, UNet demonstrates improved efficiency compared to other complex models when applied to our specific dataset of lumbar CTs, particularly due to its regularity and limited scale. Hence, UNet is selected as the baseline model for our task.

At this juncture, we have taken only a small step forward. Given that our objective necessitates precise segmentation of CT images from various hospitals, it is imperative for our model to possess robustness. Motivated by this, we improve the network’s structure and training algorithm by leveraging the proposed **SAS** framework, which is the main content of the supplementary material and is covered in detail in the following subsection.

B.2 SAS Framework

Due to the limited accurately labeled data, training a model capable of strong generalization and reliable segmentation results is challenging. This difficulty is particularly prominent in the medical field, where various imaging machines, such as different CT machine settings, can result in disparate data distributions, further complicating the problem examined in this paper. As state-of-the-art models are not applicable to the few-shot learning scenario, we aim to enhance the model’s robustness through a superior training paradigm. To achieve this, we investigated cutting-edge techniques to complement existing methods and developed a self-supervised pre-training framework called **SAS**, which consists of a Self-supervised learning framework, robust data **A**ugmentations, and a **S**patial deformation network. Furthermore, **SAS** can be easily integrated into CNN models, enabling the substitution of UNet with any specific CNN model for medical vision problems.

B.2.1 Self-supervised Contrastive Pre-training

Dan et al. [33] demonstrated that applying self-supervised learning to an image dataset enhances the robustness and generalization ability of deep learning models. Hence, inspired by [34, 35], we pre-train the model with memory bank contrastive learning (Figure 10) before proceeding with training using the supervised target.

In particular, for an input image, we generate two variations using a series of random data augmentations, referred to as the *query* and *key* respectively. Both are then passed to the model backbone, resulting in corresponding activations. We store the previous activations of the *key* in a memory bank and randomly select a subset as negative samples during subsequent iterations. Next, we calculate the contrastive loss, or InfoNCE loss, using the *query* activation, *key* activation, and negative samples in the following manner:

$$\mathcal{L}_q = -\log \frac{\exp(q^T k_+ / \tau)}{\sum \exp(q^T k_i / \tau)}, \quad (4)$$

where q represents the *query* activation, k_+ denotes the *key* activation, k_i corresponds to the negative samples, and τ represents a temperature hyper-parameter. A lower temperature prioritizes the separation of the *query* from the hardest negative samples. Typically, a relatively lower temperature is chosen, as documented in [36, 34]. By rewarding the closeness between query and (positive) key and penalizing the closeness between the query and negative samples, the contrastive pre-training empowers the model to identify the similarities between images by embedding them into a lower-dimensional representational space. Further details of the contrastive pre-training algorithm are provided in Algorithm 1.

The model extracts high-level semantic representations from variations of an image, referred to as positive samples. Variations are obtained through image transformations like rotation, flipping, and color space conversions. Simultaneously, the model captures semantic representations of random irrelevant images, referred to as negative samples. The model is trained to embed images into a low-dimensional space by maximizing the differences between these two types of representation vectors. After initializing the model parameters, the model is fine-tuned on the labeled dataset to enhance both the accuracy and the stability of the segmentation result.

B.2.2 Data Augmentation

Data augmentation is a widely adopted training technique in deep learning, with [37, 38, 39] suggesting that data augmentation enhances the robustness of deep neural networks. Therefore, we employ multiple data augmentation methods, including random brightness, contrast, and hue alteration, to expand our training sample collections and expose

[†]The code and models are publicly available at <https://github.com/THU-CVlab/JMedSegV2>

The changing rule of human bone density with aging based on a novel definition and mensuration of bone density with computed tomography

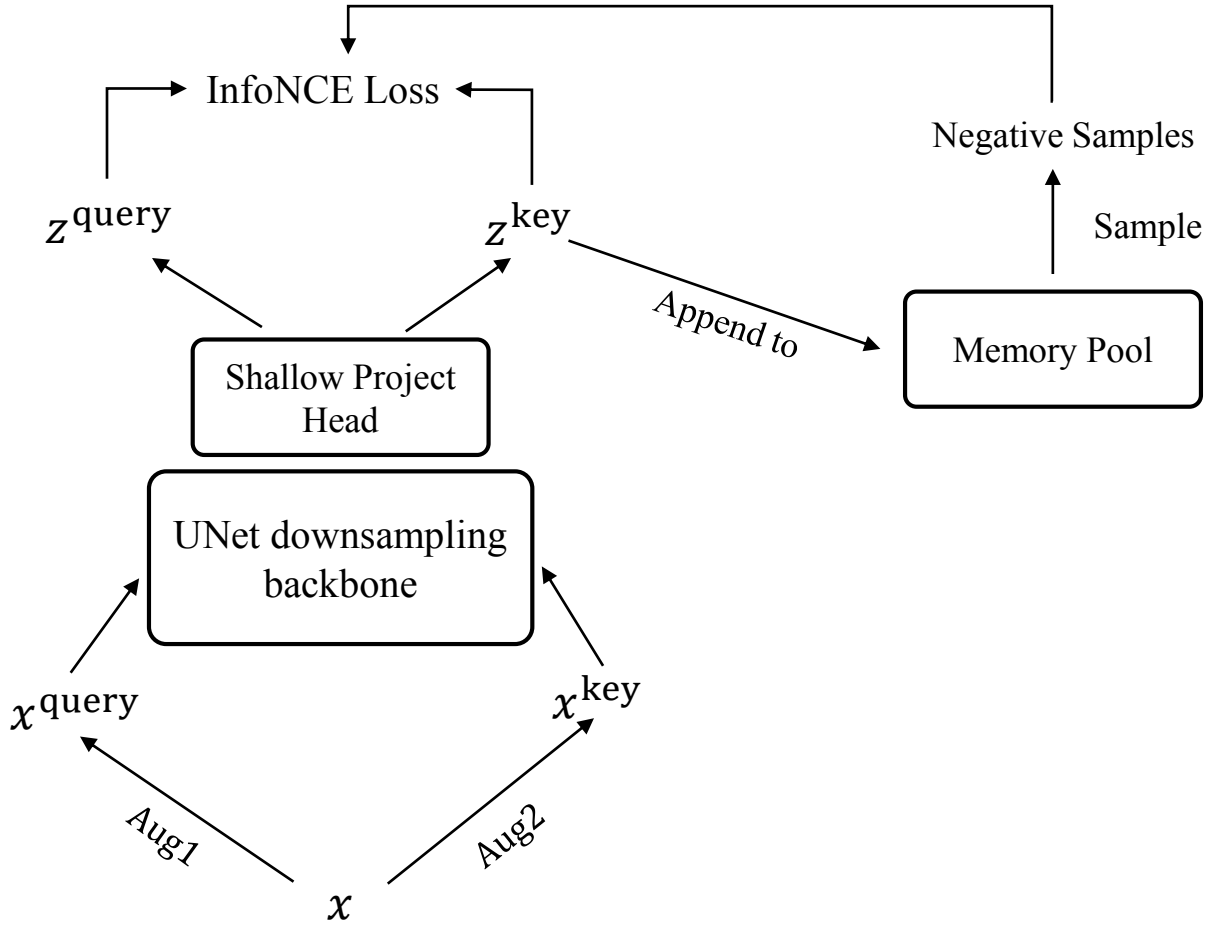


Figure 10: The constrastive learning pre-train framework.

Algorithm 1 Contrastive Pre-training

Input: model f , parameters Θ , input image x , random augmentation ϕ , memory pool M , learning rate η .

Output: Pretrained model f .

- 1: $x_q \leftarrow \phi(x)$
 - 2: $x_k \leftarrow \phi(x)$
 - 3: $q \leftarrow f(x_q)$
 - 4: $k \leftarrow f(x_k)$
 - 5: Random sample K negative samples k_i from M
 - 6: Disable the gradient computation of k_i and q
 - 7: Compute \mathcal{L}_q according to Equation 4
 - 8: Update the parameters by $\Theta \leftarrow \Theta - \eta \nabla_{\Theta} \mathcal{L}_q$;
-

the model to an augmented dataset. We do not employ geometric deformations such as random rotation or cropping because modifying the segmentation label alongside image transformation could potentially disrupt the continuity and regularity of the segmentation mask and negatively affect the model’s performance. Instead, we employ an implicit approach to implement geometric transformations, avoiding label manipulation while significantly enhancing the model’s robustness (further details are provided in the subsequent paragraphs).

B.2.3 Spatial Transformer Network

Jaderberg et al. [40] introduced the Spatial Transformer Network (STN), which automatically aligns an image’s geometric features by learning an adaptive affine transformation. The localization network, a shallow CNN, outputs a

The changing rule of human bone density with aging based on a novel definition and mensuration of bone density with computed tomography

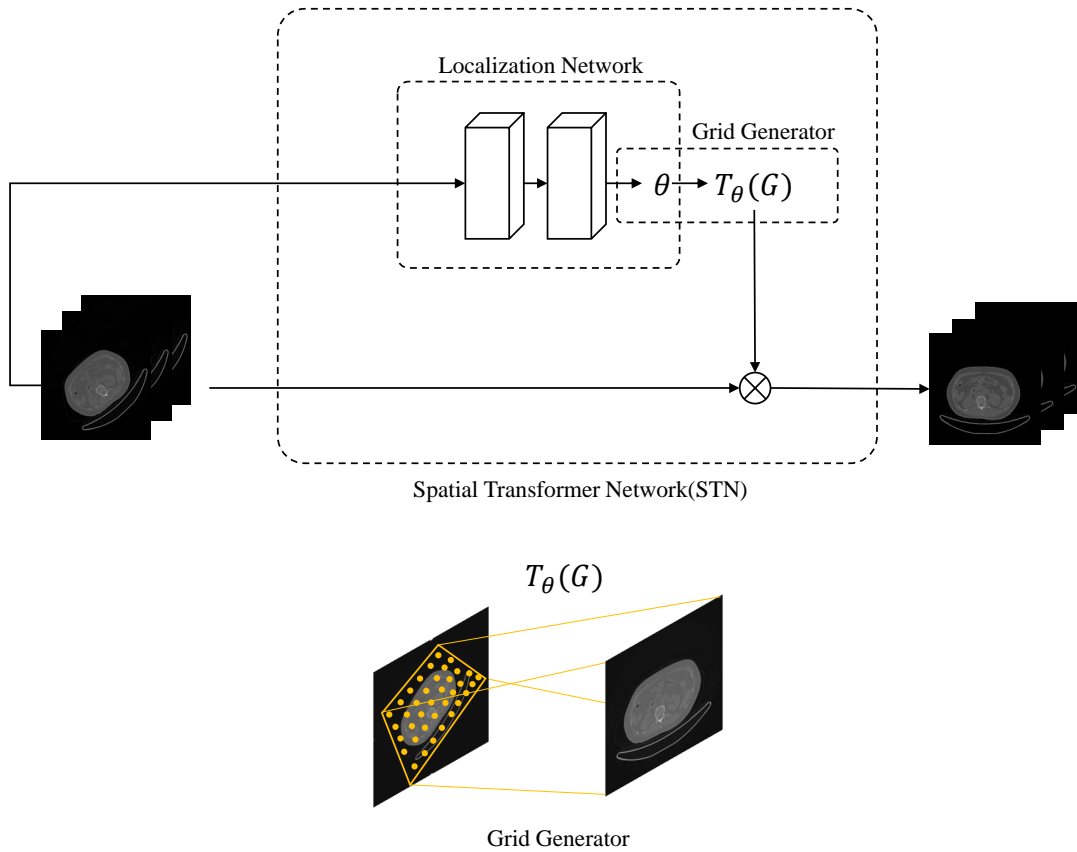


Figure 11: Illustration of the spatial transformer network.

2×3 matrix, which, combined with Eq. (5), allows for obtaining the corresponding pixel location in the original image associated with a specific transformed pixel. Subsequently, bilinear interpolation calculates the precise pixel value.

$$\begin{pmatrix} x_i^s \\ y_i^s \end{pmatrix} = \begin{pmatrix} \theta_{11} & \theta_{12} & \theta_{13} \\ \theta_{21} & \theta_{22} & \theta_{23} \end{pmatrix} \begin{pmatrix} x_i^t \\ y_i^t \\ 1 \end{pmatrix} \quad (5)$$

The STN can be integrated into any CNN for end-to-end training, including UNet. STN can improve the regularity of the image dataset and contribute to more accurate segmentation results, considering discrepancies in medical equipment placement and variations in posture. For instance, if a person is not in a lying position and the CT scan of their lumbar bone is misaligned, a well-trained model’s performance on such CT scans may be underwhelming. However, by utilizing STN and heavily augmented data, the model can correct these geometric deformations and achieve superior results.

The localization network utilized in our experiment consists of multiple layers of CNN blocks. Each block includes a 3×3 2D convolutional layer, a BatchNorm layer, and a ReLU activation function. At the end of the network, an AveragePool layer is included to accommodate different resolutions. Here we provide the Jittor-style code for the STN.

```
import numpy as np
import jittor as jt
import jittor.nn as nn
from jittor.init import constant_

class BasicBlock(nn.Module):
    def __init__(self, in_c, out_c):
```

The changing rule of human bone density with aging based on a novel definition and mensuration of bone density with computed tomography

```

        self.model = nn.Sequential(
            nn.Conv2d(in_c, out_c, kernel_size=3, padding=1),
            nn.BatchNorm2d(out_c),
            nn.ReLU()
        )
    def execute(self, x):
        return self.model(x)

class STNWrapper(nn.Module):
    def __init__(self, convnet):
        self.convnet = convnet # unet or any CNN
        self.loc = nn.Sequential(
            BasicBlock(3, 8), BasicBlock(8, 16),
            BasicBlock(16, 32), BasicBlock(32, 64),
            nn.AdaptiveAvgPool2d(2)
        )
        self.fc_loc = nn.Sequential(
            nn.Linear(256, 32), nn.ReLU(), nn.Linear(32, 6)
        )
        constant_(self.fc_loc[2].weight, 0.)
        constant_(self.fc_loc[2].bias, np.array([1., 0., 0., 0., 1., 0.]))

    def stn(self, x):
        # the localization network will output a 2x3 affine matrix
        xs = self.loc(x)
        xs = xs.view(-1, 256)
        theta = self.fc_loc(xs)

        # generate the mapped coordinates
        theta = theta.view(-1, 2, 3)
        grid = nn.affine_grid(theta, x.size())

        # sample with bilinear interpolation
        z = nn.grid_sample(x, grid)
        return z

    def execute(self, x):
        z = self.stn(x) # perform deformation with the stn function defined
        y = self.convnet(z) # pass it to the unet
        return y

```

B.2.4 Complete Pipeline

The SAS training framework consists of two stages. In the first stage, we employ Algorithm 1 for contrastive self-supervised pre-training to initialize the model backbone. Following the pre-training, we utilize the labels for supervised training, where we enhance the UNet by incorporating the STN structure and applying color space data augmentations.

B.3 Experiment and Result

B.3.1 Training Details

For the self-supervised contrastive pre-training, the UNet model is trained for 50 iterations using the Adam optimizer and a learning rate of 5×10^{-6} . The predefined semantic representations are generated by the fourth down-sampling layer of the UNet model, resulting in 512-channel feature maps. The pre-training is performed with a batch size of four, and the temperature hyper-parameter (τ) in Eq. 4 is set to the default value of 0.07.

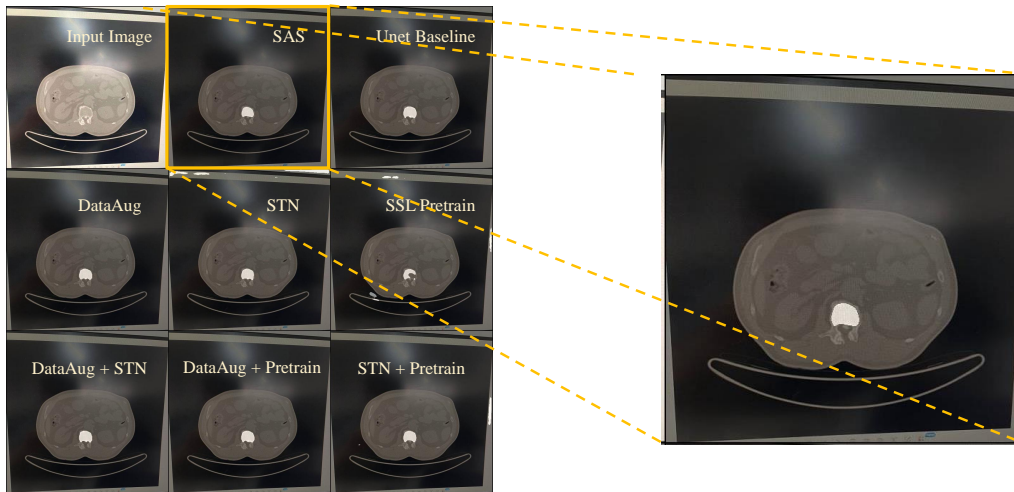
During supervised training, the model is trained with the Adam optimizer with a learning rate of 3×10^{-4} for 50 iterations. The batch size is set to four as well.

B.3.2 Ablation Experiment on SAS

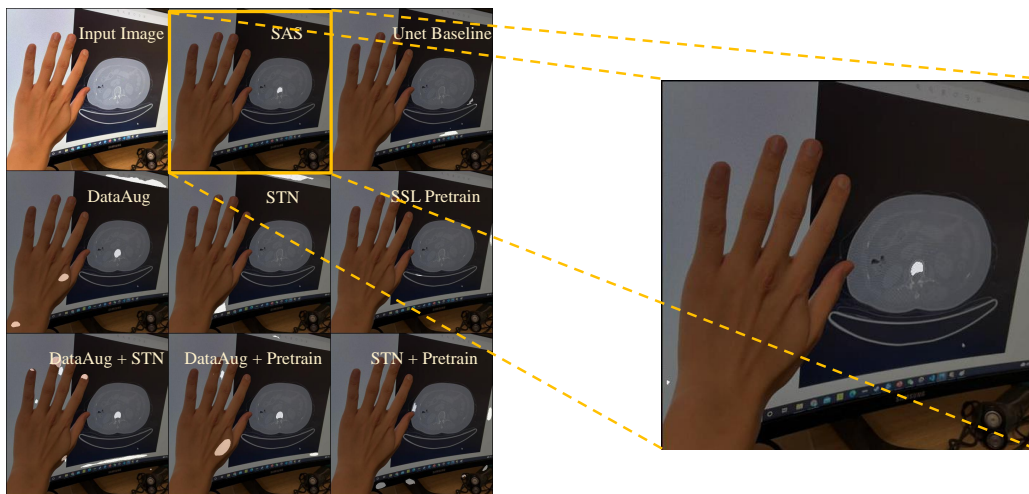
Initially, an ablation study is conducted on our SAS components, and qualitative results are obtained. To evaluate the generalization performance of the segmentation models, a photograph of a CT scan displayed on a computer screen

The changing rule of human bone density with aging based on a novel definition and mensuration of bone density with computed tomography

is captured using a mobile phone and used as the input. The respective results are depicted in Figure 12. In cases where the image suffers from slight distortion or corruption, all methods exhibit similar performance. However, when additional visual semantic elements are introduced, resulting in greater spatial deformation and color deviation, our SAS framework demonstrates a significant advantage over competitor methods.



(a) A photo of the CT scan image shot with smartphone (b) A close-up look of SAS framework result in (a)



(c) Another smartphone photo, with more spatial deformation and interfering visual elements (hand, computer) (d) A close-up look of SAS framework result in (c)

Figure 12: Results on the ablation experiment, where *input image* denotes the CT scan photograph, and *(SSL) Pretrain*, *STN*, *DataAug* refers to the self-supervised contrastive pre-training, spatial transformer network and color space data augmentation, respectively. *SAS* is our SAS training framework, and *UNet Baseline* is the basic UNet structure without extra training techniques.

All tested models undergo training using the same medical image data and a UNet backbone. The obtained results demonstrate the effectiveness of the SAS training framework in enhancing the robustness and generalization performance of medical image segmentation models when faced with limited training samples. Moreover, this framework ensures precise segmentation of the lumbar bone.

B.3.3 Quantitative and Qualitative Result

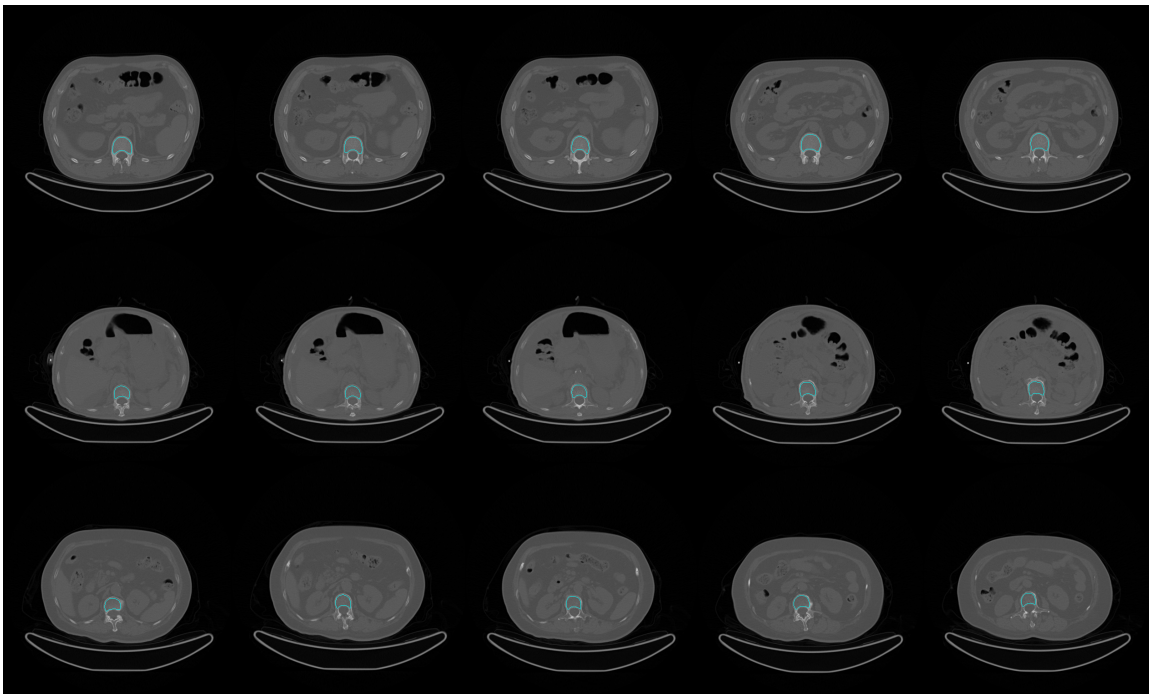
In this experiment, a quantitative analysis of the test dataset is performed. The segmentation result metrics of UNet, trained using the SAS training framework, are presented in Table 3. The high prediction and recall rates demonstrate that the model’s prediction ability aligns with the professional doctors’ segmentation results.

The segmentation results are visualized in Figure 13. Each row of lumbar spine CT scans represents a single person, with the lumbar spine from L1 to L2 displayed from left to right. Due to the varying CT machine settings between the N and S Hospitals, there is a difference in the size of lumbar vertebrae, with larger sizes observed in the S Hospital and smaller sizes in the N Hospital. Nonetheless, the SAS framework demonstrates remarkable robustness, enabling accurate segmentation in both hospitals. Furthermore, the generated contours are smooth, and their accuracy surpasses that of manual labeling, thereby offering a more reliable segmentation result for subsequent analysis. The area of the lumbar cancellous bones acquired using our model will be utilized for further analysis of bone density.

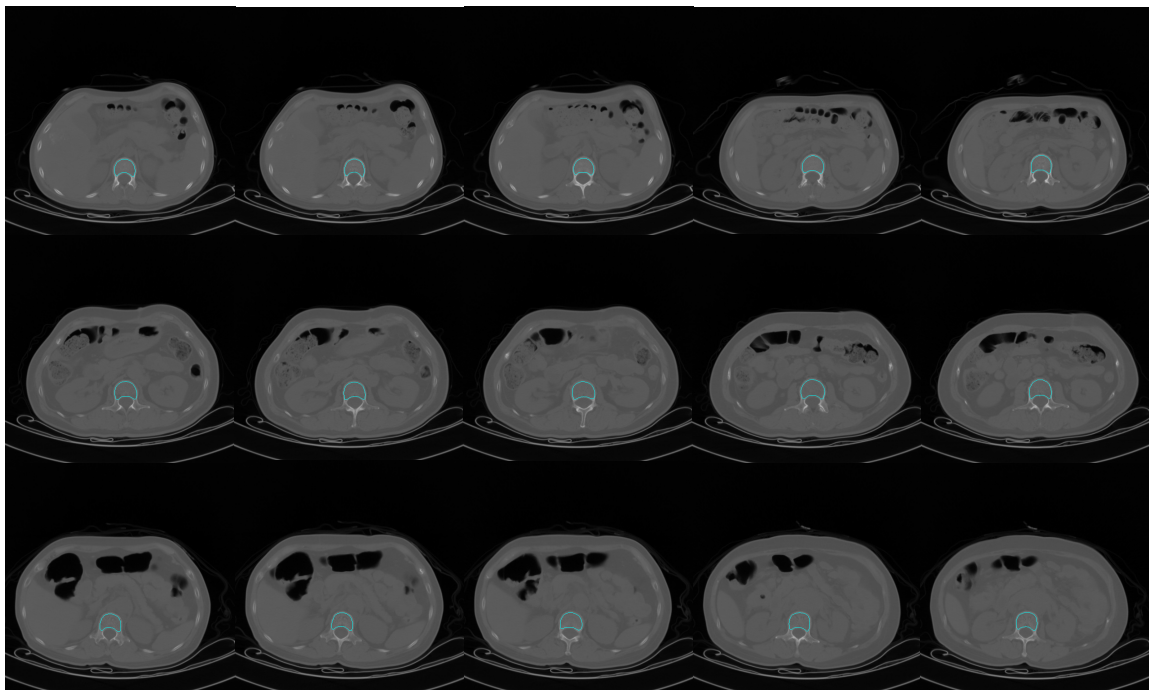
Table 3: Quantitative results on the test dataset.

Metrics	Mean Dice	Mean IoU	Accuracy	Recall
Result	0.97985	0.96124	0.99811	0.99959

The changing rule of human bone density with aging based on a novel definition and mensuration of bone density with computed tomography



(a) N Hospital



(b) S Hospital

Figure 13: Visualizing the segmentation results obtained by the UNet model trained with our SAS framework.

References

- [1] Catherine Bree Johnston and Meenakshi Dagar. Osteoporosis in older adults. *Medical Clinics*, 104(5):873–884, 2020.
- [2] Rosa Lorente-Ramos, Javier Azpeitia-Armán, Araceli Muñoz-Hernández, José Manuel García-Gómez, Patricia Díez-Martínez, and Miguel Grande-Báñez. Dual-energy x-ray absorptiometry in the diagnosis of osteoporosis: a practical guide. *AJR-American Journal of Roentgenology*, 196(4):897, 2011.
- [3] HH Bolotin and H Sievänen. Inaccuracies inherent in dual-energy x-ray absorptiometry in vivo bone mineral density can seriously mislead diagnostic/prognostic interpretations of patient-specific bone fragility. *Journal of bone and mineral research*, 16(5):799–805, 2001.
- [4] Claudie Berger, Lisa Langsetmo, Lawrence Joseph, David A Hanley, K Shawn Davison, Robert Josse, Nancy Kreiger, Alan Tenenhouse, David Goltzman, et al. Change in bone mineral density as a function of age in women and men and association with the use of antiresorptive agents. *Cmaj*, 178(13):1660–1668, 2008.
- [5] Hugo Giambini, Sundeep Khosla, Ahmad Nassr, Chunfeng Zhao, and Kai-Nan An. Longitudinal changes in lumbar bone mineral density distribution may increase the risk of wedge fractures. *Clinical Biomechanics*, 28(1):10–14, 2013.
- [6] Fernando U Kay, Vinh Ho, Edmund B Dosunmu, Avneesh Chhabra, Keenan Brown, Xinhui Duan, and Orhan K Öz. Quantitative computed tomography detects undiagnosed low bone mineral density in oncologic patients imaged with f-18-fdg-pet/ct. *Clinical nuclear medicine*, 46(1):8, 2021.
- [7] Xiaoguang Chen, Liang Wang, Qiang Zeng, and Jing Wu. The china guideline for the diagnosis of osteoporosis with quantitative coputed tomography (2018). *Chinese Journal of Osteoporosis*, 13(3):6, 2019.
- [8] Cristina Panaroni, Andrew J Yee, and Noopur S Raje. Myeloma and bone disease. *Current osteoporosis reports*, 15:483–498, 2017.
- [9] Marianna L Oppenheimer-Velez, Hugo Giambini, Asghar Rezaei, Jon J Camp, Sundeep Khosla, and Lichun Lu. The trabecular effect: A population-based longitudinal study on age and sex differences in bone mineral density and vertebral load bearing capacity. *Clinical Biomechanics*, 55:73–78, 2018.
- [10] Xiong-Fei Pan, Limin Wang, and An Pan. Epidemiology and determinants of obesity in china. *The lancet Diabetes & endocrinology*, 9(6):373–392, 2021.
- [11] Shi-Min Hu, Dun Liang, Guo-Ye Yang, Guo-Wei Yang, and Wen-Yang Zhou. Jittor: a novel deep learning framework with meta-operators and unified graph execution. *Science China Information Sciences*, 63(222103):1–21, 2020.
- [12] Quanwei Huang, Yuezhi Zhou, Linmi Tao, Weikang Yu, Yaoxue Zhang, Li Huo, and Zuoxiang He. A chinese model based on the markov chain for unsupervised medical image segmentation. *Tsinghua Science and Technology*, 26(6):833–844, 2021.
- [13] Ego Seeman and TJ Martin. Antiresorptive and anabolic agents in the prevention and reversal of bone fragility. *Nature Reviews Rheumatology*, 15(4):225–236, 2019.
- [14] PL Jager, S Jonkman, W Koolhaas, A Stiekema, BHR Wolffenbuttel, and RHJA Slart. Combined vertebral fracture assessment and bone mineral density measurement: a new standard in the diagnosis of osteoporosis in academic populations. *Osteoporosis international*, 22:1059–1068, 2011.
- [15] L Joseph Melton III, B Lawrence Riggs, Tony M Keaveny, Sara J Achenbach, David Kopperdahl, Jon J Camp, Peggy A Rouleau, Shreyasee Amin, Elizabeth J Atkinson, Richard A Robb, et al. Relation of vertebral deformities to bone density, structure, and strength. *Journal of Bone and Mineral Research*, 25(9):1922–1930, 2010.
- [16] DR Sarvamangala and Raghavendra V Kulkarni. Convolutional neural networks in medical image understanding: a survey. *Evolutionary intelligence*, pages 1–22, 2021.
- [17] Kai Han, Yunhe Wang, Hanting Chen, Xinghao Chen, Jianyuan Guo, Zhenhua Liu, Yehui Tang, An Xiao, Chunjing Xu, Yixing Xu, et al. A survey on vision transformer. *IEEE Transactions on Pattern Analysis and Machine Intelligence*, 2022.
- [18] Ruiyang Liu, Yinghui Li, Dun Liang, Linmi Tao, Shimin Hu, and Hai-Tao Zheng. Are we ready for a new paradigm shift? a survey on visual deep mlp. *arXiv preprint arXiv:2111.04060*, 2021.
- [19] Ruiyang Liu, Yinghui Li, Linmi Tao, Dun Liang, and Hai-Tao Zheng. Are we ready for a new paradigm shift? a survey on visual deep mlp. *Patterns*, 3(7), 2022.

- [20] Olaf Ronneberger, Philipp Fischer, and Thomas Brox. U-net: Convolutional networks for biomedical image segmentation. In *International Conference on Medical image computing and computer-assisted intervention*, pages 234–241. Springer, 2015.
- [21] Thorsten Falk, Dominic Mai, Robert Bensch, Özgün Çiçek, Ahmed Abdulkadir, Yassine Marrakchi, Anton Böhm, Jan Deubner, Zoe Jäckel, Katharina Seiwald, et al. U-net: deep learning for cell counting, detection, and morphometry. *Nature methods*, 16(1):67–70, 2019.
- [22] Fabian Isensee, Jens Petersen, Andre Klein, David Zimmerer, Paul F Jaeger, Simon Kohl, Jakob Wasserthal, Gregor Koehler, Tobias Norajitra, Sebastian Wirkert, et al. nnu-net: Self-adapting framework for u-net-based medical image segmentation. *arXiv preprint arXiv:1809.10486*, 2018.
- [23] Hao Dong, Guang Yang, Fangde Liu, Yuanhan Mo, and Yike Guo. Automatic brain tumor detection and segmentation using u-net based fully convolutional networks. In *annual conference on medical image understanding and analysis*, pages 506–517. Springer, 2017.
- [24] Pablo Gómez, Andreas M Kist, Patrick Schlegel, David A Berry, Dinesh K Chhetri, Stephan Dürr, Matthias Echternach, Aaron M Johnson, Stefan Kniesburges, Melda Kunduk, et al. Bagls, a multihospital benchmark for automatic glottis segmentation. *Scientific data*, 7(1):1–12, 2020.
- [25] Zongwei Zhou, Md Mahfuzur Rahman Siddiquee, Nima Tajbakhsh, and Jianming Liang. Unet++: A nested u-net architecture for medical image segmentation. In *Deep learning in medical image analysis and multimodal learning for clinical decision support*, pages 3–11. Springer, 2018.
- [26] Huimin Huang, Lanfen Lin, Ruofeng Tong, Hongjie Hu, Qiaowei Zhang, Yutaro Iwamoto, Xianhua Han, Yen-Wei Chen, and Jian Wu. Unet 3+: A full-scale connected unet for medical image segmentation. In *ICASSP 2020-2020 IEEE International Conference on Acoustics, Speech and Signal Processing (ICASSP)*, pages 1055–1059. IEEE, 2020.
- [27] Xuebin Qin, Zichen Zhang, Chenyang Huang, Masood Dehghan, Osmar R Zaiane, and Martin Jagersand. U2-net: Going deeper with nested u-structure for salient object detection. *Pattern Recognition*, 106:107404, 2020.
- [28] Liang-Chieh Chen, George Papandreou, Iasonas Kokkinos, Kevin Murphy, and Alan L Yuille. Deeplab: Semantic image segmentation with deep convolutional nets, atrous convolution, and fully connected crfs. *IEEE transactions on pattern analysis and machine intelligence*, 40(4):834–848, 2017.
- [29] Foivos I Diakogiannis, François Waldner, Peter Caccetta, and Chen Wu. Resunet-a: A deep learning framework for semantic segmentation of remotely sensed data. *ISPRS Journal of Photogrammetry and Remote Sensing*, 162:94–114, 2020.
- [30] Sijing Cai, Yunxian Tian, Harvey Lui, Haishan Zeng, Yi Wu, and Guannan Chen. Dense-unet: a novel multiphoton in vivo cellular image segmentation model based on a convolutional neural network. *Quantitative imaging in medicine and surgery*, 10(6):1275, 2020.
- [31] Jun Fu, Jing Liu, Haijie Tian, Yong Li, Yongjun Bao, Zhiwei Fang, and Hanqing Lu. Dual attention network for scene segmentation. In *Proceedings of the IEEE/CVF Conference on Computer Vision and Pattern Recognition*, pages 3146–3154, 2019.
- [32] Sixiao Zheng, Jiachen Lu, Hengshuang Zhao, Xiatian Zhu, Zekun Luo, Yabiao Wang, Yanwei Fu, Jianfeng Feng, Tao Xiang, Philip HS Torr, et al. Rethinking semantic segmentation from a sequence-to-sequence perspective with transformers. In *Proceedings of the IEEE/CVF Conference on Computer Vision and Pattern Recognition*, pages 6881–6890, 2021.
- [33] Dan Hendrycks, Mantas Mazeika, Saurav Kadavath, and Dawn Song. Using self-supervised learning can improve model robustness and uncertainty. *arXiv preprint arXiv:1906.12340*, 2019.
- [34] Kaiming He, Haoqi Fan, Yuxin Wu, Saining Xie, and Ross Girshick. Momentum contrast for unsupervised visual representation learning. In *Proceedings of the IEEE/CVF Conference on Computer Vision and Pattern Recognition*, pages 9729–9738, 2020.
- [35] Ting Chen, Simon Kornblith, Mohammad Norouzi, and Geoffrey Hinton. A simple framework for contrastive learning of visual representations. In *International conference on machine learning*, pages 1597–1607. PMLR, 2020.
- [36] Zhirong Wu, Yuanjun Xiong, Stella X Yu, and Dahua Lin. Unsupervised feature learning via non-parametric instance discrimination. In *Proceedings of the IEEE conference on computer vision and pattern recognition*, pages 3733–3742, 2018.
- [37] Zach Eaton-Rosen, Felix Bragman, Sebastien Ourselin, and M Jorge Cardoso. Improving data augmentation for medical image segmentation. 2018.

The changing rule of human bone density with aging based on a novel definition and mensuration of bone density with computed tomography

- [38] Connor Shorten and Taghi M Khoshgoftaar. A survey on image data augmentation for deep learning. *Journal of Big Data*, 6(1):1–48, 2019.
- [39] Cherry Khosla and Baljit Singh Saini. Enhancing performance of deep learning models with different data augmentation techniques: A survey. In *2020 International Conference on Intelligent Engineering and Management (ICIEM)*, pages 79–85. IEEE, 2020.
- [40] Max Jaderberg, Karen Simonyan, Andrew Zisserman, et al. Spatial transformer networks. *Advances in neural information processing systems*, 28:2017–2025, 2015.